# Models for Dense Molecular Cloud Cores

Steven D. Doty and David A. Neufeld
Department of Physics and Astronomy, The Johns Hopkins University
3400 N. Charles St., Baltimore, MD 21218

### **ABSTRACT**

We present a detailed theoretical model for the thermal balance, chemistry, and radiative transfer within quiescent dense molecular cloud cores that contain a central protostar. In the interior of such cores, we expect the dust and gas temperatures to be well coupled, while in the outer regions CO rotational emissions dominate the gas cooling and the predicted gas temperature lies significantly below the dust temperature. Large spatial variations in the gas temperature are expected to affect the gas phase chemistry dramatically; in particular, the predicted water abundance varies by more than a factor of 1000 within cloud cores that contain luminous protostars.

Based upon our predictions for the thermal and chemical structure of cloud cores, we have constructed self-consistent radiative transfer models to compute the line strengths and line profiles for transitions of <sup>12</sup>CO, <sup>13</sup>CO, C<sup>18</sup>O, orthoand para- $\mathrm{H}_{2}^{16}\mathrm{O},$  ortho- and para- $\mathrm{H}_{2}^{18}\mathrm{O},$  and OI. We carried out a general parameter study to determine the dependence of the model predictions upon the parameters assumed for the source. We expect many of the far-infrared and submillimeter rotational transitions of water to be detectable either in emission or absorption with the use of the *Infrared Space Observatory* (ISO) and the Submillimeter Wave Astronomy Satellite. Quiescent, radiatively-heated hot cores are expected to show low-gain maser emission in the 183 GHz  $3_{13} - 2_{20}$ water line, such as has been observed towards several hot core regions using ground base telescopes. We predict the  ${}^{3}P_{1}$  -  ${}^{3}$  P<sub>2</sub> fine structure transition of atomic oxygen near 63  $\mu$ m to be in strong absorption against the continuum for many sources. Our model can also account successfully for recent ISO observations of absorption in rovibrational transitions of water toward the source AFGL 2591.

Subject headings: ISM: clouds — ISM: molecules — molecular processes — masers — radiative transfer — radio lines: ISM

#### 1. Introduction

The role of dense molecular clouds as the sites of star formation has been clearly established (e.g. Shu, Adams, & Lizano 1987, and references therein). Although the evolution of cloud cores from the onset of collapse to fragmentation and star formation is not completely understood, the collapse process is partly regulated by the ability of the core to cool itself. A full understanding of the thermal balance within molecular cloud cores requires a careful consideration of the microphysics of molecular excitation, cloud core chemistry, and radiative transfer.

Goldsmith and Langer (1978) carried out a comprehensive study of radiative cooling in dense molecular clouds, computing the cooling rates from a number of molecules as a function of molecular hydrogen density and gas temperature. Neufeld, Lepp, and Melnick (1995, hereafter NLM) re-examined the cooling rates using the molecular cooling functions obtained by Neufeld and Kaufman (1993, hereafter NK) and included the effects of gas phase chemistry. They also predicted line strengths for many important species (e.g. H<sub>2</sub>O & CO) for the ideal case of an isothermal cloud core in hydrostatic equilibrium, and argued that much of the energy radiated by the gas in molecular cloud cores emerges in far-infrared and submillimeter transitions that are detectable only from satellite observatories. More recently, Ceccarelli, Hollenbach & Tielens (1996, hereafter CHT) have presented a model for collapsing cloud cores in which the chemistry, thermal balance, and line emission were treated simultaneously.

These recent theoretical developments have been motivated in large part by rapid advances in observational capabilities. The recent launch of the Infrared Space Observatory and the planned launch of the Submillimeter Wave Astronomy Satellite (SWAS) will allow the far-infrared and submillimeter spectral regions to be probed without any hindrance by the Earth's atmosphere. These satellite observatories will therefore afford us an ideal opportunity to study transitions for which the atmospheric absorption is severe, such as molecular oxygen transitions and far-infrared water transitions. Although emission in several submillimeter water transitions has been observed from ground-based telescopes or airborne observatories (e.g., Waters et al. 1980; Phillips et al. 1980; Wannier et al. 1991; Jacq et al. 1988; Cernicharo et al. 1990, 1994; Gensheimer et al. 1996; Zmuidzinas et al. 1996; Tauber et al. 1996), such observations typically probe transitions which play a negligible role in the thermal balance of the emitting gas. SWAS and ISO, by contrast, will allow the dominant cooling transitions of dense molecular cloud cores to be studied. ISO will also allow vibrational bands of molecules to be observed in absorption toward bright infrared sources. For example, recent ISO observations by Helmich et al. (1996), and by van Dishoeck & Helmich (1996) of the  $\nu_2$  vibrational band of water in absorption toward

several protostars provide an important constraint on the abundance of water relative to other species.

Motivated by these observational developments, we have constructed a detailed theoretical model for dense molecular cloud cores, obtaining a self-consistent solution for the thermal balance, chemistry, and radiative transfer at every point within a spherical cloud core. After determining the radial distribution of the dust and gas temperatures and the chemical composition, we computed self-consistently the line strengths and line profiles for relevant transitions of astrophysically important molecules. We have considered a large grid of models in order to explore a wide range of possible source parameters; in particular, the present study extends the work of CHT to the case of cloud cores with embedded protostars of very high luminosity.

In §2 we describe our model for dense molecular cloud cores and discuss the microphysical processes that were included. In §3, we discuss the results obtained for a standard set of parameters relevant to a hot core region such as the Orion Molecular Cloud 1. In §4 we consider a grid of models covering the entire range of cloud core masses and protostellar luminosities that are applicable to star-forming regions in the Galaxy. In §5 we discuss the results of this parameter study in light of current and upcoming observational capabilities. A brief summary follows in §6.

#### 2. Model

We have modeled the dense, quiescent, star-forming cores of molecular clouds. We assume that the cores are spherical, and – as our standard assumption – that the molecular hydrogen density follows an  $r^{-2}$  distribution, consistent with both observations (Goldsmith et al. 1980, Keto et al. 1988, Myers & Fuller 1992, Fuller & Myers 1993) and the fact that theoretical models of star formation (e.g. Larson 1969) predict evolution toward an  $r^{-2}$  distribution even for a homogeneous initial state. We have also carried out additional test calculations with an alternate  $r^{-1.5}$  density distribution, with results which are described in §3.6 below. The cloud core is assumed to have inner and outer radii at which the  $H_2$  densities are  $10^9$  cm<sup>-3</sup> and  $10^3$  cm<sup>-3</sup> respectively, although these limits can be changed significantly with little effect on the emission for most transitions. The microturbulent doppler parameter,  $\Delta v$ , and the exact density profile are determined from considerations of hydrostatic equilibrium as discussed by Neufeld & Green (1994). Given the standard  $r^{-2}$  density distribution, we are left with two source parameters: the gas density at some reference point (or equivalently the total mass M(< d), enclosed within a region of diameter d), and the internal source luminosity,  $L_*$ .

Once the mass enclosed (and hence gas density) and source luminosity, have been specified, the temperature structure and line emission may be determined. Our model – represented schematically in Figure 1 – includes careful consideration of the thermal balance, chemistry and radiative transfer within the cloud core. These are discussed below.

#### 2.1. Thermal Balance

The equilibrium gas temperature within the cloud core is determined by the balance between heating and cooling processes.

The gas heating is dominated by gas-grain collisional heating. Dust grains within the core are heated both from the inside by the central protostar and from the outside by the interstellar radiation field; inelastic collisions then transfer energy from the warmer dust grains to the gas. We determined the dust temperature from a self-consistent solution of the continuum radiative transfer problem (§2.3 below), and then used the estimate of Hollenbach & McKee (1989) for the rate of collisional energy transfer to the gas.

We adopted the cooling functions of NLM to determine the gas cooling rates due to emissions from CO,  $O_2$ , OI,  $H_2$ ,  $H_2O$  as well as from other diatomic and polyatomic molecules. The NLM results are based upon the use of an approximate escape probability method to treat the effects of radiative trapping in optically thick cooling transitions, and neglect the effects of pumping by infrared continuum radiation. They have been tabulated by NLM as a function of the gas density, the gas temperature, and an optical depth parameter denoted  $\widetilde{N}$ .

In the outer regions of dense cloud cores, where radiative cooling causes the gas temperature to fall significantly below the dust temperature, carbon monoxide is the dominant coolant. We have therefore used a full radiative transfer code employing the method of approximate lambda iteration (ALI, c.f. §2.4 below) to determine the CO cooling in detail for comparison with the NLM cooling functions. We find that exact CO cooling rate is well approximated by the expression

$$\Lambda_{\rm CO} = \left[ \Lambda_{\rm NLM}(T_{\rm gas}) - \Lambda_{\rm NLM}(2.7K) \right] \tag{1}$$

evaluated for an optical depth parameter (c.f. NK)

$$\widetilde{N} = 0.5 N_{\rm CO} / \Delta v,$$
 (2)

where  $\Lambda_{\rm NLM}$  is the NLM cooling function for CO,  $N_{\rm CO}$  is the CO column density along a radial path to the cloud surface, and  $\Delta v$  is the Doppler parameter. The second term in

equation (1) accounts for the effects of heating by the 2.7 K cosmic background radiation. Note also that the best fit to the ALI results was obtained with the optical depth parameter taken as  $0.5N_{\rm CO}/\Delta v$ , a factor of 2 below the value recommended by NK for the case of a spherical cloud with a  $r^{-2}$  density profile. With these modifications to the NLM cooling function, we derived an equilibrium gas temperature that agreed everywhere to within 1 K with the results obtained using the ALI radiative transfer code to treat CO cooling exactly.

Similar ALI calculations were also carried out for water and OI. They showed that in cores with an embedded protostar of high luminosity, absorption by water and atomic oxygen could actually lead to net heating of the gas (confirming a conclusion reached earlier by Takahashi, Hollenbach & Silk (1983) for the case of water transitions in hot core regions). However, water and OI transitions were found to have a significant effect upon the radiative cooling rate only deep in the cloud interior where the gas temperature was in any case very closely coupled to the dust temperature.

In the very outer parts of the cloud, grain photoelectric heating and cosmic ray heating may be significant relative to gas-grain collisional heating. Neither of these processes is included in our present study, so the gas temperature near the outer edge of the cloud may have been somewhat underestimated.

# 2.2. Chemistry

We adopted the steady-state molecular abundances that were computed by NLM, who included the full UMIST chemical network (Millar et al. 1991, Farquhar & Millar 1993) and assumed the initial gas-phase elemental abundances of Millar et al. (1991, Table 4). While this approach has the benefit of being easily calculable, the consideration of only steady-state gas-phase chemistry may underestimate the abundances of volatile ices such as water and methanol that have been recently vaporized from grain surfaces in hot core regions. On the other hand, water is predicted to be very abundant in any case for gas temperatures greater than  $\sim 300$  K, so the neglect of time-dependent and grain-surface chemical effects will have a significant effect upon the predicted water abundance only in a relatively small region where the gas temperature is smaller than 300 K but the dust temperature exceeds the sublimation temperature of water ice ( $\sim 100$  K). As our standard assumption, we therefore ignore the complications of time-dependent chemical effects and the desorption of icy grain mantles in the present study. We have, however, performed test calculations to investigate what effects upon the line strengths are likely to result from the desorption of icy grain mantles above 100 K; as described in §3.6 below, the effects are relatively small.

#### 2.3. Continuum Radiative Transfer

A detailed treatment of the radiative transfer through dust is necessary to correctly determine the dust temperature (and hence the gas temperature; see §2.1), as well as the infrared pumping and emergent spectrum. We adopt dust properties that are based upon Draine's (1987) astronomical silicate in the visible through mid-infrared spectral regions ( $\lambda < 25~\mu\text{m}$ ), with an assumed grain size of  $a = 0.1~\mu\text{m}$ . For  $\lambda > 25~\mu\text{m}$ , we assume a dust opacity  $\propto \lambda^{-1.5}$  for all models, and we adopt a normalization for the dust opacity corresponding to  $N(\text{H}_2)/A_V \sim 2 \times 10^{21}\,\text{cm}^{-2}$  (Bohlin et al 1978, Whittet 1992). Given specified parameters for the cloud core (viz.  $L_*$ ,  $M_{0.1}$ ) and these assumed optical properties for the dust, we used a modified version of the continuum radiative transfer code of Egan, Leung, & Spagna (1988) to solve self-consistently for the dust emissivity, opacity, and temperature as functions of position.

#### 2.4. Line Radiative Transfer

Given the radial distribution of gas density, molecular abundance, and gas temperature, we are able to determine the level populations and emergent line intensities for molecules of interest in hot core regions. This is accomplished through the self-consistent solution of the radiation transport problem in 1-D spherical geometry using a code (Doty 1997) based on the approximate lambda iteration (ALI) method proposed by Rybicki & Hummer (1992). Along with the spatial variations in the gas parameters, our code also includes the effects of dust absorption and emission (as determined from the continuum radiative transfer model).

In formulating the equations of statistical equilibrium for the molecular level populations, we adopted the same spontaneous radiative rates and collisional rate coefficients used by NLM, except in the case of water, for which new estimates of the collisional rate coefficients have recently become available. In particular, Phillips et al. (1995) have obtained the first estimates of the inelastic collision cross-sections for the  $\rm H_2-H_2O$  system, yielding rate coefficients at temperatures  $T<140~\rm K$  for collisionally induced transitions among the lowest ten rotational states of ortho– and para-water as a result of collisions with either  $\rm H_2$  (J=0) or  $\rm H_2$  (J=1). Thus whereas NLM simply assumed that the earlier collision cross-sections computed by Green, Maluendes, and McLean (1993) for the He–H<sub>2</sub>O system applied also to  $\rm H_2-H_2O$ , in the present study we have used the actual results of Phillips et al. (1995) for  $\rm H_2-H_2O$  collisions. Assuming that cloud cores were initially cold ( $T<20\rm K$ ) and in local thermodynamic equilibrium, and that the time since the formation of an internal heat source (i.e. protostar) has been short in comparison to the para-H<sub>2</sub> to ortho-H<sub>2</sub> conversion time (>  $10^6$  yr according to Abgrall et al. 1992),

we expect that molecular hydrogen will be almost entirely in the para (J=0) state. We therefore adopted the rate coefficients computed by Phillips et al. (1995) for the excitation of water by  $H_2$  (J=0); these typically lie within a factor 2 of the corresponding values for excitation of  $H_2O$  by He. For comparison, we have also performed test calculations with an assumed 3:1 ratio of ortho- to para- $H_2$ ; as described in §3.6, the strengths of most water lines show only a relatively weak dependence on the assumed ortho- to para- $H_2$  ratio.

In the calculations presented here, we have included just nine transitions involving the lowest seven rotational states for both ortho- and para-water. The relatively small number of water states included in our standard model makes it practical to compute a large grid of models. Test calculations involving up to 45 rotational states have shown that our seven-level model yields predicted line strengths for the nine transitions we considered that lie well within 5% of those derived from models that include a much larger number of rotational states.

#### 3. Results for the Standard Model

We have constructed a computer model to solve simultaneously for the gas and dust temperatures, molecular abundances and radiative transfer within a static dense molecular cloud core with an  $r^{-2}$  density profile. In this section (§3) we describe the results obtained for a "standard" model with parameters applicable to a high luminosity "hot core" region. In the next section (§4) we present the results of a general parameter study.

Our cloud core model has two input parameters: the mass enclosed in a given diameter, M(< d), and the internal source luminosity,  $L_*$ . Here we discuss a "standard" model with  $M_{0.1} \equiv M(< 0.1 \text{ pc}) = 60 \text{ M}_{\odot}$  and  $L_* = 10^5 \text{ L}_{\odot}$ . Although this model has parameters similar to the Orion hot core, direct comparison of our model with observations of Orion is not possible due to the extremely complicated nature of the Orion region. For example, our present level of detail cannot include the effects of shocks, molecular outflows, irregular geometry, clumping, and multiple heat sources – all of which are known to exist in the Orion region (Genzel & Stutzki 1989 and references therein). We expect however, that our results can be compared to observations for both simpler, more regular sources, and for some general source-averaged properties.

### 3.1. Dust temperature distribution

As noted earlier, we self-consistently solve the radiative transfer problem through the dust. In Figure 2, we compare the resulting model continuum spectrum (dashed line), to observations of Orion (Erickson et al. 1977, and references therein; filled circles) for the cloud core parameters of the standard model. It should be noted that the mid- and far-infrared opacity ( $\propto \lambda^{-1.5}$ ) we have assumed (§2.3) provides a significantly better fit to the observational data than does the dust opacity of Draine (1987).

In addition to determining the infrared continuum emission, the dust temperature affects the gas-grain heating rate (c.f. §2.1). In Figure 3 we plot the dust temperature (dashed line) as a function of radial position for this model. The dust in the interior is heated by the enclosed radiation source, while the dust on the outside is heated by the interstellar radiation field (ISRF), which we take from Mathis, Mezger & Panagia (1983). The dip in the dust temperature near  $r \sim 3-5 \times 10^{16}$  cm is due to the fact that at this point the thermal dust radiation can begin to escape easily, thereby cooling the dust and decreasing the temperature.

#### 3.2. Gas temperature distribution

Once the source properties and dust temperature distribution have been specified, the gas temperature distribution may be determined by considerations of thermal balance as described in §2.1. The resulting gas temperature profile is plotted in Figure 3 (solid line) for the standard model. The dust and gas temperatures are well coupled in the interior of the cloud core (for  $r < 10^{17}$  cm), because the gas-grain collisional energy transfer is very effective at high densities and because the large column densities to the cloud surface lead to radiative trapping of the molecular line emissions that cool the gas. At larger radii, line emissions can escape more readily and the effectiveness of gas-grain heating diminishes, thereby allowing the gas and dust to decouple thermally and the gas temperature to drop significantly below the dust temperature.

#### 3.3. Abundances

Simultaneously with the gas temperature, the gas phase chemical abundances are also determined using the steady-state solution of the UMIST reaction set (see Figure 1). The resulting fractional abundances for our standard model are shown in Figure 4, for CO (solid line), OI (dotted line), and ortho-H<sub>2</sub>O (dashed line). The predicted water abundance, in

particular, shows a strong spatial variation. In the cloud interior, where the gas temperature is greater than 300 K, water is formed rapidly by the neutral-neutral reactions:

$$O + H_2 \rightleftharpoons OH + H,$$
 (3)  
 $OH + H_2 \rightleftharpoons H_2O + H.$ 

This reaction sequence accounts for the large predicted abundance of water for  $r < 2-3 \times 10^{16}$  cm in our model, and the correspondingly low abundances of atomic oxygen. In the cool exterior, however, the forward reactions in equation (3) are slow due to the substantial activation energies involved, and the water abundance is significantly smaller; at low temperatures, water is formed only by a less effective ion-molecule reaction route that is driven by cosmic ray ionization.

### 3.4. Molecular line cooling

In Figure 5, we show the cooling coefficients ( $\equiv \Lambda/n^2[\mathrm{H}_2]$ ) for the various important coolants in our model as a function of radial position. CO dominates the cooling throughout most of the cloud core (i.e. for  $r > 2 \times 10^{16}$  cm), with  $\mathrm{O}_2$ , polyatomic molecules, and other diatomic molecules playing increasingly smaller roles. For  $r < 1 - 2 \times 10^{16}$  cm,  $\mathrm{H}_2$  and polyatomic molecules dominate the cooling, the high gas temperature allowing the effective excitation of  $\mathrm{H}_2$  vibrational emissions and the high column density favoring emission from polyatomic molecules that possess rich rotational spectra with many lines.

### 3.5. Line emission

In Figure 6, we plot the line luminosities for  $^{12}$ CO,  $^{13}$ CO, and  $^{18}$ O, as a function of upper rotational number,  $J_u$ . The results shown in Figure 6 apply to the standard model, and are presented in tabular form in Table 1. Line strengths for rotational transitions of ortho- and para- $^{16}$ O and - $^{18}$ O appear in Tables 2 and 3. Although the abundances of the isotopomers  $^{13}$ CO and  $^{18}$ O are assumed to lie factors of 100 and 500 below the abundance of  $^{12}$ CO, the predicted  $^{13}$ CO and  $^{18}$ O line luminosities are smaller than the corresponding  $^{12}$ CO line luminosities by factors of only 2–6 and 5–20 respectively, a behavior that clearly reflects optical depth effects. Similarly, the ratio of  $^{12}$ O to  $^{18}$ O line strengths are typically much smaller than the assumed abundance ratio of 500. At short wavelengths, corresponding to  $J_u$  larger than  $\sim$  20 for CO, the dust radiation field becomes increasingly important and the rotational transitions are predicted to be absorption lines.

Tables 1–3 also show the comparison between the line strength predictions of this work and those obtained by NLM for a highly idealized "hot core" model. For many lines the predicted luminosities are substantially different. The NLM hot core model differed from the standard model discussed here in several important respects. Most importantly, NLM assumed a constant gas temperature of 100 K, rather than the spatially varying temperature profile obtained from the self-consistent calculations reported here. Furthermore, NLM made use of an approximate escape probability method rather than an exact ALI method in obtaining line strength predictions, and did not include the interaction between line radiation and infrared dust continuum radiation. Finally, the assumed outer radius for the NLM was a factor 4 smaller than that assumed here.

For transitions (such as CO J=1-0) that are excited in the very outer regions of the cloud core, the predictions obtained in this study are larger than those of NLM because of the larger outer radius that we have assumed. Transitions of intermediate excitation, however, are typically predicted to show weaker emission than that predicted by NLM, the temperature in 97% of the core's mass being lower than the 100 K value adopted by NLM. On the other hand, transitions with very high critical densities (such as the water transitions originating in  $2_{21}$ ,  $3_{03}$ ,  $3_{12}$  and  $3_{21}$  levels) probe the innermost parts of the cloud core where our model predicts temperatures larger than 100 K; for these lines the NLM model therefore underpredicted the emission line luminosities relative to the standard model presented here.

Table 4 shows the predicted luminosities for the far-infrared fine structure lines of atomic oxygen. As discussed in §5.1 below, the  ${}^{3}P_{0}$  – ${}^{3}$   $P_{1}$  transition near 146  $\mu$ m is predicted to be a strong emission line and the  ${}^{3}P_{1}$  – ${}^{3}$   $P_{2}$  transition near 63  $\mu$ m to be a strong absorption line, contrary to the predictions of the recent model of CHT.

To compare simultaneously the line strengths of the dominant species, in Figure 7 we plot the spectrum of our standard model for  $^{12}$ CO,  $H_2^{16}$ O and OI lines, as well as the continuum. Here we assume a spectral resolution  $\lambda/\Delta\lambda=10^4$  and a distance to the source of 1 kpc. Notice that many of the CO lines have large line to continuum flux ratios. It is also clear that the low energy water transitions are predicted to be in emission, while the high-lying transitions are in strong absorption against the continuum.

Our model predicts a population inversion and low-gain maser amplification in one transition: the  $3_{13}-2_{20}$  transition of water near 183 GHz, which has the largest line/continuum ratio of any water line. Low-gain maser emission has indeed been observed in this transition toward several hot core regions (Cernicharo et al. 1994). Our model demonstrates that quiescent, radiatively-heated hot cores are expected to show low-gain maser emission in the 183 GHz  $3_{13}-2_{20}$  water line with a luminosity that can easily account

for (in fact, exceed by a factor of  $\sim 4$ ) that observed toward Orion-KL. Further discussion of the 183 GHz and other masing transitions will appear in a future paper (Doty & Neufeld 1997).

Our use of an ALI method to model the transfer of line radiation leads straightforwardly to predictions for the spectral line profiles. In Figures 8–11, we show emergent line profiles (assuming a beam much larger than the source) for a total of 32 transitions of ortho- $H_2^{16}O$ , ortho- $H_2^{18}O$ , para- $H_2^{16}O$ , para- $H_2^{18}O$ , and atomic oxygen. These figures show the monochromatic luminosity,  $L_{\nu}$ , as a function of Doppler shift from line center. While some transitions are pure emission or pure absorption lines, many transitions show the "self-reversed" (or "double-peaked") profiles that are characteristic of line radiation for which the source function decreases along the line-of-sight towards the observer. This behavior arises because material of low excitation temperature in the outer parts of the cloud core absorbs line radiation that was emitted by the hot, dense interior.

### 3.6. Effect of Model Assumptions

We have carried out test calculations in order to investigate the effects of changing some of the physical assumptions underlying our model. In particular, we varied the assumed gas density distribution, considered the effect of H<sub>2</sub>O desorption from icy mantles above 100K, and varied the assumed ratio of ortho- to para-H<sub>2</sub> as a collision partner with water. All these calculations were carried out for the assumed core mass and source luminosity of the standard model.

In these test calcuations, the greatest differences in the predicted line strengths occurred when we changed the assumed density distribution from  $r^{-2}$  to  $r^{-1.5}$  (while leaving the inner and outer radii and the quantity  $M_{0.1}$  unchanged). For the three CO isotopes, the typical (i.e. median) change in the predicted line strengths was  $\sim 25$  percent, with the greatest differences occurring for low-lying transitions. The typical differences in the water line strengths were  $\sim 40$  percent for o-H<sub>2</sub><sup>16</sup>O and  $\sim 70$  percent for p-H<sub>2</sub><sup>18</sup>O. For the two SWAS target lines of water, the predicted strength of the 557 GHz ortho-water line increased by 33 percent with the shallower density profile, while that of the 547 GHz para-water line decreased by a factor  $\sim 6$ . The high-lying water absorption lines were relatively unaffected, and changes in the predicted OI line strengths were smaller than 25 percent (with the 63  $\mu$ m transition still in absorption).

Next, we considered the effect of including desorption of H<sub>2</sub>O from icy grain mantles above 100K. Were carried out test calculations in which, following CHT, we assumed that

10 percent of the total oxygen was injected into the gas phase as H<sub>2</sub>O once the grain temperature exceeded 100 K. This change resulted in relatively small differences in the predicted water line strengths, with typical increases of 7, 50, 16, and 39 percent for transitions of o-H<sub>2</sub><sup>16</sup>O, o-H<sub>2</sub><sup>18</sup>O, p-H<sub>2</sub><sup>16</sup>O, and p-H<sub>2</sub><sup>18</sup>O respectively. No line strength increased by more than a factor 2.4, and the predicted strengths of the two SWAS water target lines increased 21 percent (557 GHz) and 34 percent (547 GHz) when the grain mantle desorption was included.

Finally, we have considered the effect of changing the ortho- to para- $H_2$  ratio to 3:1. For most transitions, the differences were minimal, yielding median differences in the predicted line strengths of  $\sim 10$  percent. For the two SWAS water target lines, however, the effects were atypically large, with the predicted line strengths increasing by 88 percent (557 GHz) and 77 percent (547 GHz) when the 3:1 ratio was adopted.

### 4. General Parameter Study

We have extended the calculations described in §3 to include a general parameter study of cloud cores with masses  $M_{0.1}$  in the range  $1-1000 \text{ M}_{\odot}$  that contain central sources of luminosity  $L_*$  in the range  $1-10^6 \text{ L}_{\odot}$ . We considered a total of 21 combinations of  $M_{0.1}$  and  $L_*$ , as specified in Table 5.

#### 4.1. Gas and Dust Temperature

Because the gas and dust temperature distributions play a large role in determining the emergent spectrum, we have shown in Figure 12 the gas (solid line) and dust (dashed-line) temperature distributions for our entire grid of models. In this figure, each box corresponds to a given value of  $M_{0.1}$ , while each set of lines is labeled by  $\log_{10}(L_*)$ . As in the standard model, the gas and dust temperatures are always well-coupled in the interior, but diverge in the exterior of the cloud. We note also that the gas and dust temperatures are not necessarily monotonic, due to the existence of both internal and external heat sources.

#### 4.2. Line luminosities

In Figures 13–17, we present the predicted luminosities for a total of 44 radio, submillimeter, and far-infrared lines of  $^{12}$ CO, ortho- $H_2^{16}$ O, ortho- $H_2^{18}$ O, para- $H_2^{16}$ O, para- $H_2^{18}$ O, and atomic oxygen. Each box within these figures shows the line luminosity for a

single transition, for each of the 20 models in our grid. The different symbols correspond to the different value of  $M_{0.1}$ : open triangles, open squares, crosses, and open circles represent  $M_{0.1}=1,\,10,\,10^2$ , and  $10^3\,\mathrm{M}_\odot$  respectively. For each transition, the upper panel in each full box corresponds to net emission against the background, while the lower panel corresponds to net absorption. The upper and lower panels of each box share the same zero. In Figure 18, we show the CO rotational lines strengths as a function of the upper rotational quantum number,  $J_u$ , for the case  $L_*=100\,\mathrm{L}_\odot$ . For subset of the models that we considered (with  $M_{0.1}=100\,\mathrm{M}_\odot$  and  $L_*=100\,\mathrm{L}_\odot$ ) the data are also presented in tabular form in Tables 6 & 7, along with predictions for rotational lines of  $^{13}\mathrm{CO}$  and  $^{18}\mathrm{O}$ . The entire dataset is available from the authors in computer-readable form.

The results of our parameter study show several general features. Low-lying transitions (viz. CO J=1-0, CO J=2-1, CO J=3-2 and ortho-H<sub>2</sub>O  $1_{10}-1_{01}$ ) show line luminosities that are almost independent of the central luminosity,  $L_*$ , because they are excited primarily in the outer parts of the cloud where the heating is dominated by the ISRF rather than by the central protostar. The line luminosities for such transitions increase roughly as the total assumed area of the cloud core, which is proportional to  $M_{0.1}^{3/2}$  (c.f. Neufeld & Green 1994). The line luminosities predicted by our model for low-lying transitions may be slight underestimates, due to our neglect of grain photoelectric heating.

In contrast, high-lying transitions show predicted line strengths that are increasing functions of  $L_*$ , because they originate in the cloud interior where the gas and dust temperatures increase with increasing central luminosity. We expect many such transitions to be observed in absorption against the continuum radiation emitted by dust, particularly in high-mass cloud cores. For  $^{12}$ CO, there is always a value of  $J_u$  beyond which the rotational transitions are all absorption lines: these values are tabulated in Table 8. We also note that for certain source parameters, the CO line luminosities can be a rather complex function of  $J_u$ , with line emission predicted for low- $J_u$  transitions, line absorption for intermediate- $J_u$  transitions, line emission again for transitions of yet higher  $J_u$ , and finally absorption again for the highest  $J_u$  transitions. This behavior, which is apparent in Figure 18, can occur when the gas temperature profile is non-monotonic.

#### 5. Discussion

#### 5.1. Comparison with previous studies

The main differences between the model presented here and the highly-idealized hot core models of NLM have been discussed in §3.5 above. Despite the quantitative differences

between the results obtained from the two models, the present study confirms the *qualitative* result of NLM that far-infrared and submillimeter lines dominate the emission from gas in dense molecular cloud cores.

Another detailed model for the thermal and chemical structure within – and line emission from – dense molecular cloud cores was presented recently by CHT, for the case of cores containing low-mass protostars of luminosity 20 or 65  $L_{\odot}$ . Our present study greatly expands the range of  $L_*$  and  $M_{0.1}$  considered, and makes use of a ALI radiative transfer method rather than the approximate escape probability approach adopted by CHT. On the other hand, the model of CHT included four effects that are not considered in the present work. First, CHT treated the cloud chemistry in a time-dependent manner, following the chemical evolution of water and other species after they vaporized from icy grain mantles (c.f. §2.2 above.). Second, CHT considered the effects of velocity gradients in the cloud core, using the collapse solution of Shu (1977) to specify the evolution of the density profile and infall velocities. Third, CHT found that compressional heating can be important in the core interior; we do not include this process as we do not include the infall of material. Finally, CHT included vibrational pumping by near-infrared photons, a process that we have neglected. In the static case that we have considered, the vibrational pumping rate will be significantly dimished by radiative trapping, in contrast to the infall case considered by CHT where the pumping photons could propagate due to a spatial velocity gradient.

In general, our study agrees with many of the qualitative results of CHT, except in the prediction of OI  $^3P_1$  –  $^3P_2$  line emission. In particular, while CHT predicted that this line should be a strong emission line, we find that the  $^3P_1$  –  $^3P_2$  OI line should be in absorption for a wide range of source parameters. This difference arises because the temperature profile in the CHT model is higher due to their inclusion of compressional heating. In our model, the predicted absorption is also enhanced due to our more extended envelopes and our assumption of constant line widths.

As a check, we have used our ALI code to determine the expected line strengths for a cloud core with the same temperature profile, density profile, and linewidths assumed by CHT. We find the OI 63  $\mu$ m line to be in *emission* for that case, deriving fluxes for this and other lines that agree to within a factor of 1.5 - 5 with the CHT results. The CHT predictions are consistently larger than our corresponding ALI results, a behaviour which we believe – results from CHT's use of an approximate escape probability method for the line transfer.

Although beyond the scope of this paper, it is interesting to consider the possible implications of the transition of the  ${}^{3}P_{1} - {}^{3}P_{2}$  OI line from emission (CHT) to absorption (this study). In particular, over a wide range of parameters it appears that quiescent

sources without the infall of material are predicted to exhibit absorption in this line, while collapsing sources are predicted to show net emission. Further study on the effects of a velocity gradient and compressional heating are needed to understand the range of applicability of this result. If the result is robust, then the simple presence of emission in the 63  $\mu$ m OI line might serve as a collapse signature.

## 5.2. Observational implications: far-IR and submillimeter lines

Many of the far-infrared and submillimeter transitions that we expect to be characteristic of dense molecular cloud cores lie at wavelengths for which ground-based observations are made impossible by the effects of atmospheric absorption. NLM have emphasized the crucial role that airborne and satellite observatories will play in testing our models for dense cloud cores; these observatories include the recently-launched *Infrared Space Observatory* (ISO), the *Submillimeter Wave Astronomy Satellite* (SWAS, scheduled for launch in 1997), and the planned *Stratospheric Observatory for Infrared Astronomy* (SOFIA).

ISO, SWAS and SOFIA have complementary observational capabilities. ISO provides an ideal platform for the study of far-infrared transitions of  $\mathrm{H}_2^{16}\mathrm{O}$  and high-J ( $J_u > 13$ ) CO transitions, although at a spectral resolution ( $\sim 30\,\mathrm{km\,s^{-1}}$  in the  $45-180\,\mu\mathrm{m}$  range) that will not allow the line profiles from quiescent cores to be resolved. SWAS, by contrast, will carry out high spectral resolution ( $\sim 0.6\,\mathrm{km\,s^{-1}}$ ) observations of 5 spectral lines in the  $487-557\,\mathrm{GHz}$  frequency range: the  $1_{10}-1_{01}$  lines of  $\mathrm{H}_2^{16}\mathrm{O}$  and  $\mathrm{H}_2^{18}\mathrm{O}$ ; the  $^3\mathrm{P}_1-^3\mathrm{P}_0$  fine structure line of atomic carbon; the J=5-4 line of  $^{13}\mathrm{CO}$ , and the 3(3)-1(2) line of molecular oxygen. With a primary mirror of diameter 4 times as large as that of either ISO or SWAS, SOFIA will provide much better spatial resolution than any previous airborne or infrared satellite observatory, and with appropriate instrumentation will cover much of the infrared and submillimeter spectral region. However, even at a flying altitude of 14 km, atmospheric attenuation will severely limit SOFIA's ability to observe water or molecular oxygen. For all three observatories, detailed cloud core models such as those presented in this study will be essential in deriving molecular abundances from the line strengths that are observed.

Finally, we note that many transitions that are unobservable from the ground for Galactic sources are shifted into atmospheric windows for high redshift galaxies. Thus far, CO rotational emissions have been detected unequivocally from three high redshift systems: the Cloverleaf (at z=2.551; Barvainis, et al. 1992, Barvainis, et al. 1994, Hewitt & Burbidge 1989), the ultraluminous IR galaxy F10214+4724 (at z=2.286; Brown & Vanden Bout 1991, Downes, Solomon, & Radford 1993) and a companion (a gaseous nebula

at z=4.702; Petitjean, et al. 1996) to the quasar BR1202-0725. Searches for water in these sources would provide a valuable probe of the chemistry and molecular excitation at high redshift. Prime target lines for these sources are listed in Table 9, along with their appropriate redshift. In the two nearest sources, the  $2_{11} - 2_{02}$  water line, redshifted to 228.9 GHz in F10214+4724 and to 211.8 GHz in the Cloverleaf, should be the strongest observable line. In the companion to BR1202-0725, the strongest line should be the  $3_{21} - 3_{12}$  water line (redshifted to 203.9 GHz), with many others also expected to be strong – a prediction which is robust for a relatively wide range of model parameters.

### 5.3. Observational implications: mid-IR vibrational absorption bands

Although the present study has emphasized molecular rotational lines and atomic fine structure lines at submillimeter and far-infrared wavelengths, ISO also affords us the opportunity of studying vibrational absorption bands in the near- and mid-infrared spectral region. In particular, recent ISO observations by Helmich et al. (1996), and by van Dishoeck & Helmich (1996, hereafter vDH) have led to the detection of the  $\nu_2$  vibrational band of water vapor near 6  $\mu$ m in absorption toward several protostars.

For the source GL 2591, vDH estimated the water abundance by assuming that the absorption takes place in an isothermal region that lies entirely in front of – and completely covers – the source of 6  $\mu$ m continuum emission. That assumption leads to an estimate of  $2 \times 10^{18}$  cm<sup>-2</sup> for the water column density. Given a CO column density that has been estimated by a similar method as  $2 \times 10^{19}$  cm<sup>-2</sup> (Mitchell et al. 1989, 1990), and an assumed CO abundance relative to H<sub>2</sub> of  $2 \times 10^{-4}$ , vDH derived a mean water vapor abundance of  $2 \times 10^{-5}$  along the line-of-sight to GL 2591.

In our cloud core models, the predicted strength of the  $\nu_2$  absorption band is complicated by several effects. First, the model predicts strong spatial variations in the water abundance. Second, the water vapor that is responsible for the  $\nu_2$  band absorption is largely cospatial with the dust that gives rise to the 6  $\mu$ m continuum emission. Third, the source is assumed to have a spherical (rather than a plane-parallel) geometry.

For comparison with the water vapor column density inferred from the simpler analysis of vDH, we have computed an *effective* water column density for our cloud core models. To do so, we defined an effective photosphere for the 6  $\mu$ m radiation, and computed the beam-averaged (and intensity-weighted) water column density from the cloud surface to that photosphere. Table 10 shows the effective column densities thereby derived for the  $\nu_2$  band of water, as well as for the  $\nu_2 = 0$  band of CO. Given estimates of  $\sim 50\,\mathrm{M}_\odot$  for

 $M_{0.1}$  in GL 2591 (Carr et al. 1995) and  $2 \times 10^4 L_{\odot}$  for  $L_*$  (Mozurkewich, Schwartz, & Smith 1986), the results given in Table 10 are in acceptable agreement with the column densities derived from observations of GL 2591. Since our model does not include the vaporization of water from icy grain mantles, we conclude that high-temperature gas-phase chemistry in the interior of the cloud core is adequate by itself to explain the relatively large average water abundances derived by vDH. The importance of high-temperature chemistry is further supported by the relatively high excitation temperature ( $\sim 300 \text{ K}$ ) inferred by vDH, although more detailed modeling will clearly be required to obtain quantitative predictions against which the excitation temperature can be compared.

### 6. Summary

We have constructed a detailed, self-consistent model for the thermal balance, chemistry, and continuum and line radiative transfer in dense molecular cloud cores that contain a central protostar. Our model makes specific predictions about the temperature and molecular abundances as a function of radial position within such a cloud core. We have carried out a general parameter study to obtain predictions for the spectra of molecular cloud cores as a function of the cloud core mass and the luminosity of the central luminosity source. The principal results of our study may be summarized as follows:

- 1. The gas and dust temperatures are well-coupled in the dense interiors of molecular cloud cores. In the outer regions of cloud cores, however, the gas cools efficiently through CO rotational lines and the gas temperature drops significantly below the dust temperature. Furthermore, the temperature distributions need not be monotonic due to the existence of both internal and external heat sources.
- 2. Due to the existence of both temperature and density gradients, the molecular abundances are not expected to be constant within dense molecular cloud cores. In particular, the predicted  $H_2O$  abundance varies by over a factor of 1000 in our models.
- 3. We have obtained predictions for the strengths of a large number of transitions of <sup>12</sup>CO, <sup>13</sup>CO, C<sup>18</sup>O, ortho- and para-H<sub>2</sub><sup>16</sup>O, ortho- and para-H<sub>2</sub><sup>18</sup>O, and atomic oxygen. In general, we find that the lowest lying transitions are generally emission lines with strengths that are almost independent of the central luminosity. Higher lying transitions, by contrast, generally show line strengths that are proportional to the central luminosity and are often predicted to be absorption lines.
- 4. Many of the most prominent lines expected in the spectra of dense molecular cloud cores are unobservable from ground-based telescopes but should be readily detectable from

airborne and space-based observatories such as ISO, SWAS and SOFIA. The  $^3P_1$   $-^3$   $P_2$  fine structure line of atomic oxygen near 63  $\mu$ m is expected to be in strong absorption for many quiescent sources. Quiescent, radiatively-heated hot cores are expected to show low-gain maser emission in the 183 GHz  $3_{13}$  –  $2_{20}$  water line, such as has been observed toward several hot core regions using ground-based telescopes.

- 5. Many lines are predicted to show the "self-reversed" or "double-peaked" profiles that are characteristic of line emission from a source in which the excitation temperature decreases along the line-of-sight toward the observer.
- 6. Our model successfully accounts for the water column densities inferred by van Dishoeck and Helmich from observations of the  $\nu_2$  absorption band of water toward the source GL 2591.

We thank Ali Yazdanfar for his help in calculating the thermal balance in the gas. We are grateful to David Hollenbach and to Cecilia Ceccarelli for helpful comments. We acknowledge with gratitude the support of NASA grant NAGW-3147 from the Long Term Space Astrophysics Research Program and of a NSF Young Investigator Award to D.A.N.

Table 1: CO line luminosities for various transitions in the standard model.

	<sup>12</sup> CO	<sup>12</sup> CO	<sup>13</sup> CO	<sup>13</sup> CO	$C^{18}O$	$\mathrm{C}^{18}\mathrm{O}$
	This Work	NLM	This Work	NLM	This Work	NLM
$J=1\rightarrow 0$	4.3(-3)	1.8(-3)	2.3(-3)	2.5(-4)	7.1(-4)	6.2(-5)
$2 \rightarrow 1$	2.1(-2)	1.5(-2)	1.4(-2)	5.0(-3)	5.0(-3)	1.6(-3)
$3 \rightarrow 2$	4.9(-2)	5.1(-2)	2.9(-2)	2.3(-2)	1.1(-2)	8.6(-3)
$4 \rightarrow 3$	8.8(-2)	1.2(-1)	4.1(-2)	5.7(-2)	1.5(-2)	2.3(-2)
$5 \rightarrow 4$	1.3(-1)	2.2(-1)	4.9(-2)	1.1(-1)	1.8(-2)	4.2(-2)
$6 \rightarrow 5$	1.6(-1)	3.8(-1)	5.3(-2)	1.5(-1)	2.0(-2)	5.8(-2)
$7 \rightarrow 6$	1.9(-1)	5.7(-1)	5.2(-2)	1.9(-1)	1.9(-2)	6.3(-2)
$8 \rightarrow 7$	1.9(-1)	8.2(-1)	4.9(-2)	2.0(-1)	1.8(-2)	6.2(-2)
$9 \rightarrow 8$	1.9(-1)	1.1(-0)	4.3(-2)	1.8(-1)	1.5(-2)	5.3(-2)
$10 \rightarrow 9$	1.7(-1)	1.4(-0)	3.6(-2)	1.5(-1)	1.3(-2)	4.2(-2)
$11 \rightarrow 10$	1.5(-1)	1.5(-0)	3.0(-2)	1.1(-1)	1.0(-2)	3.1(-2)
$12 \rightarrow 11$	1.1(-1)	1.3(-0)	2.2(-2)	6.7(-2)	7.5(-3)	1.8(-2)
$13 \rightarrow 12$	8.8(-2)	1.1(-0)	1.7(-2)	4.4(-2)	5.7(-3)	1.1(-2)
$14 \rightarrow 13$	6.8(-2)	7.9(-1)	1.3(-2)	2.7(-2)	4.1(-3)	6.4(-3)
$15 \rightarrow 14$	5.1(-2)	5.2(-1)	9.3(-3)	1.5(-2)	2.9(-3)	3.5(-3)
$16 \rightarrow 15$	3.7(-2)	3.2(-1)	6.6(-3)	8.1(-3)	1.9(-3)	1.7(-3)
$17 \rightarrow 16$	2.4(-2)	1.9(-1)	4.4(-3)	3.9(-3)	1.2(-3)	8.1(-4)

Note. — In this table, a(b) means  $a \times 10^b \text{ L}_{\odot}$ 

Table 2: Ortho- $H_2O$  line luminosities for various transitions in the standard model.

	o-H <sub>2</sub> <sup>16</sup> O	o-H <sub>2</sub> <sup>16</sup> O	o-H <sub>2</sub> <sup>18</sup> O	o-H <sub>2</sub> <sup>18</sup> O
	This Work	NLM	This Work	NLM
$1_{10} \to 1_{01}$	3.3(-3)	1.8(-2)	4.1(-4)	4.6(-4)
$3_{12} \rightarrow 3_{03}$	1.4(-1)	1.1(-2)	1.1(-2)	N/A
$3_{12} \rightarrow 2_{21}$	1.3(-1)	2.1(-2)	3.8(-3)	N/A
$3_{21} \rightarrow 3_{12}$	3.0(-1)	8.7(-3)	1.5(-2)	N/A
$2_{21} \rightarrow 2_{12}$	2.1(-2)	4.1(-2)	-9.7(-3)	6.0(-4)
$2_{12} \rightarrow 1_{01}$	-3.5(-1)	2.0(-1)	-6.4(-2)	3.9(-3)
$3_{03} \rightarrow 2_{12}$	-2.5(-2)	9.2(-2)	-3.2(-3)	1.7(-3)
$2_{21} \rightarrow 1_{10}$	-1.2(-0)	N/A	-9.1(-2)	N/A
$3_{21} \rightarrow 2_{12}$	-2.4(-0)	N/A	-1.3(-1)	N/A

Note. — In this table, a(b) means  $a \times 10^b \,\mathrm{L}_{\odot}$ .

Table 3: Para- $H_2O$  line luminosities for various transitions in the standard model.

	p-H <sub>2</sub> <sup>16</sup> O	p-H <sub>2</sub> <sup>16</sup> O	p-H <sub>2</sub> <sup>18</sup> O	p-H <sub>2</sub> <sup>18</sup> O
	This Work	NLM	This Work	NLM
$3_{13} \to 2_{20}$	6.8(-4)	N/A	3.0(-5)	N/A
$2_{11} \rightarrow 2_{02}$	1.1(-1)	1.3(-2)	5.0(-3)	N/A
$2_{02} \rightarrow 1_{11}$	1.9(-1)	4.9(-2)	1.1(-2)	8.4(-4)
$1_{11} \rightarrow 0_{00}$	-7.1(-2)	7.6(-2)	-7.5(-3)	1.5(-3)
$2_{20} \rightarrow 2_{11}$	2.6(-1)	8.6(-3)	9.7(-3)	N/A
$3_{22} \rightarrow 3_{13}$	3.6(-2)	1.3(-2)	-4.8(-3)	N/A
$3_{13} \rightarrow 2_{02}$	-2.6(-1)	N/A	-2.0(-2)	N/A
$2_{20} \to 1_{11}$	-1.6(-0)	N/A	-8.1(-2)	N/A
$3_{22} \rightarrow 2_{11}$	-1.2(-0)	N/A	-3.8(-2)	N/A

Note. — In this table, a(b) means  $a \times 10^b \,\mathrm{L}_{\odot}$ .

Table 4: OI line luminosities for various transitions in the standard model.

	<sup>16</sup> O	<sup>16</sup> O
	This Work	NLM
$J=0 \rightarrow 1$	9.0(-2)	N/A
$J=1 \rightarrow 2$	-1.4(-0)	N/A

Note. — In this table, a(b) means  $a \times 10^b \,\mathrm{L}_\odot$ .

Table 5: Grid of models considered in this work. "X" denotes models run.

$M_{0.1}/\mathrm{M}_{\odot}$	$1~{\rm L}_{\odot}$	$10~{\rm L}_{\odot}$	$10^2~{\rm L}_{\odot}$	$10^3~{\rm L}_{\odot}$	$10^4~{\rm L}_{\odot}$	$10^5~{ m L}_{\odot}$	$10^6~{\rm L}_{\odot}$
1	X	X	X	_	_	_	_
10	X	X	X	X			
60						Std. Model	
$10^{2}$	X	X	X	X	X	X	
$10^{3}$	X	X	X	X	X	X	X

Table 6. Background-subtracted line luminosities

Transition	Frequency (GHz)	$1~{\rm M}_{\odot}$	$10~{\rm M}_{\odot}$	$10^2~{ m M}_{\odot}$	$10^3~{ m M}_{\odot}$
<sup>12</sup> CO					
$J=1\rightarrow 0$	115.271	2.3(-6)	1.1(-4)	5.2(-3)	2.1(-1)
$4 \rightarrow 3$	461.041	5.1(-5)	9.0(-4)	1.5(-2)	2.0(-1)
$7 \rightarrow 6$	806.652	1.1(-4)	` '	1.2(-3)	` '
$10 \rightarrow 9$	1151.985	8.6(-5)	2.4(-4)	-3.5(-5)	` '
$13 \rightarrow 12$	1496.923	4.6(-5)	6.2(-5)	-7.0(-5)	-1.1(-6)
$16 \rightarrow 15$	1841.346	2.4(-5)	8.4(-6)	-1.0(-5)	-3.7(-8)
$19 \rightarrow 18$	2185.135	1.3(-5)	1.4(-7)	-2.1(-7)	-3.4(-8)
$22 \rightarrow 21$	2528.172	6.9(-6)	1.7(-6)	3.7(-9)	-2.0(-8)
$\mathrm{C^{18}O}$					
$J=1\rightarrow 0$	109.782	9.6(-7)	3.2(-5)	1.1(-3)	3.1(-2)
$4 \rightarrow 3$	439.089	1.4(-5)	` ,	1.1(-3)	2.4(-3)
$7 \rightarrow 6$	768.252	1.3(-5)	, ,	1.2(-4)	, ,
$10 \rightarrow 9$	1097.164	7.5(-6)	2.4(-5)	3.1(-6)	-1.4(-6)
$13 \rightarrow 12$	1425.718	3.7(-6)	7.3(-6)	-2.9(-8)	-5.0(-8)
$16 \rightarrow 15$	1753.805	1.6(-6)	1.7(-6)	7.1(-9)	-3.6(-8)
$19 \rightarrow 18$	2081.311	5.0(-7)	2.7(-7)	2.6(-10)	-3.4(-8)
$22 \rightarrow 21$	2408.140	1.3(-7)	3.0(-8)	-7.8(-11)	-2.0(-8)
<sup>13</sup> CO					
$J=1\rightarrow 0$	110.201	2.1(-6)	7.2(-5)	2.6(-3)	7.9(-2)
$4 \rightarrow 3$	440.765	3.1(-5)	3.8(-4)	2.4(-3)	
$7 \rightarrow 6$	771.185	3.2(-5)	` '		
$10 \rightarrow 9$	1101.353	1.8(-5)	5.1(-5)	, ,	, ,
$13 \rightarrow 12$	1431.160	9.2(-6)	, ,	-2.4(-6)	` '
$16 \rightarrow 15$	1760.499	4.8(-6)	5.0(-6)	5.0(-9)	-3.6(-8)
$19 \rightarrow 18$	2089.240	2.0(-6)	1.2(-6)	1.7(-9)	-3.4(-8)
$22 \rightarrow 21$	2417.308	5.9(-7)	1.4(-7)	-4.3(-11)	-2.0(-8)
o-H <sub>2</sub> <sup>16</sup> O					
$1_{10} \rightarrow 1_{01}$	556.936	9.2(-6)	1.5(-4)	1.1(-3)	-8.6(-3)
$3_{12} \rightarrow 3_{03}$				-5.0(-4)	
$3_{12} \rightarrow 2_{21}$	1153.127	` '	` '	-2.4(-4)	

Table 6—Continued

Transition	Frequency (GHz)	$1~{ m M}_{\odot}$	$10~{ m M}_{\odot}$	$10^2~{\rm M}_{\odot}$	$10^3~{ m M}_{\odot}$
$3_{21} \rightarrow 3_{12}$	1162.911	3.4(-5)	1.2(-4)	-1.3(-4)	-1.4(-4)
$2_{21} \rightarrow 2_{12}$	1661.008	4.3(-5)	-1.1(-4)	-2.1(-3)	5.4(-3)
$2_{12} \to 1_{01}$	1669.905	8.0(-7)	-5.7(-4)	-5.3(-3)	-1.1(-2)
$3_{03} \to 2_{12}$	1716.770	2.8(-5)	-2.7(-4)	-2.8(-3)	-1.4(-3)
$2_{21} \to 1_{10}$	2773.978	-1.2(-4)	-1.4(-3)	-2.5(-3)	-9.6(-3)
$3_{21} \rightarrow 2_{12}$	3977.047	-2.7(-4)	-1.1(-3)	-2.6(-4)	-3.4(-5)
o-H <sub>2</sub> <sup>18</sup> O					
$1_{10} \rightarrow 1_{01}$	547.676	6.6(-7)	1.1(-5)	-2.5(-5)	-5.1(-3)
$3_{12} \rightarrow 3_{03}$	1095.627	3.4(-6)	1.9(-5)	-4.3(-6)	-8.5(-6)
$3_{12} \rightarrow 2_{21}$	1181.394	1.6(-6)	5.0(-6)	-8.7(-7)	-6.5(-7)
$3_{21} \rightarrow 3_{12}$	1136.704	3.9(-6)	2.4(-5)	1.2(-5)	-1.1(-6)
$2_{21} \rightarrow 2_{12}$	1633.484	4.2(-6)	1.1(-5)	-1.3(-4)	-2.2(-5)
$2_{12} \rightarrow 1_{01}$	1655.868	-5.5(-7)	-1.9(-4)	-2.6(-3)	-3.4(-3)
$3_{03} \rightarrow 2_{12}$	1719.250	5.0(-6)	-2.6(-5)	-3.2(-4)	-4.8(-5)
$2_{21} \rightarrow 1_{10}$	2741.675	-1.4(-5)	-3.3(-4)	-7.3(-4)	-2.7(-5)
$3_{21} \rightarrow 2_{12}$	3951.581	-2.5(-5)	-1.5(-4)	-2.1(-5)	-2.7(-8)
p-H <sub>2</sub> <sup>16</sup> O					
$3_{13} \rightarrow 2_{20}$	183.310	2.3(-7)	1.2(-6)	5.5(-6)	2.4(-5)
$2_{11} \to 2_{02}$	752.033	2.5(-5)	1.5(-4)		-2.0(-3)
$2_{02} \to 1_{11}$	987.927	4.4(-5)	2.0(-4)	-8.2(-4)	
$1_{11} \to 0_{00}$	1113.344	1.4(-5)	-6.4(-5)	-3.8(-3)	-4.0(-2)
$2_{20} \rightarrow 2_{11}$	1228.789	3.5(-5)	1.2(-4)	-5.5(-4)	-4.7(-4)
$3_{22} \rightarrow 3_{13}$	1919.360	2.0(-5)	-7.7(-5)	-5.1(-4)	-1.2(-5)
$3_{13} \to 2_{02}$	2164.132	2.6(-6)	-5.5(-4)	-2.3(-3)	-2.2(-4)
$2_{20} \rightarrow 1_{11}$	2968.750	-1.5(-4)	-1.3(-3)	-1.6(-3)	-5.9(-4)
$3_{22} \rightarrow 2_{11}$	3331.459	-1.4(-4)	-9.7(-4)	-4.8(-4)	-2.8(-7)
$p-H_2^{18}O$					
$3_{13} \rightarrow 2_{20}$	203.408	8.3(-10)	2.1(-9)	2.2(-8)	1.2(-7)
$2_{11} \rightarrow 2_{02}$	745.320	1.7(-6)	2.2(-5)	6.2(-5)	-7.3(-5)
$2_{02} \rightarrow 1_{11}$			3.9(-5)		
$1_{11} \rightarrow 0_{00}$	1101.698	, ,	-2.0(-5)	, ,	, ,

Table 6—Continued

Transition	Frequency (GHz)	$1~{ m M}_{\odot}$	$10~{ m M}_{\odot}$	$10^2~{ m M}_{\odot}$	$10^3~{ m M}_{\odot}$
$2_{20} \rightarrow 2_{11}$ $3_{22} \rightarrow 3_{13}$ $3_{13} \rightarrow 2_{02}$ $2_{20} \rightarrow 1_{11}$ $3_{22} \rightarrow 2_{11}$	1199.006 1894.324 2147.733 2939.000 3296.737	3.1(-6) $2.9(-6)$ $2.0(-6)$ $-1.1(-5)$ $-5.2(-6)$	3.0(-5) $4.9(-6)$ $-4.3(-5)$ $-2.1(-4)$ $-4.8(-5)$	3.6(-5) $-4.9(-6)$ $-1.5(-4)$ $-2.8(-4)$ $-9.8(-6)$	-4.5(-6)  -1.3(-7)  -3.2(-6)  -1.8(-6)  -8.9(-9)
$\begin{array}{c} ^{16}O\\ 0 \rightarrow 1\\ 1 \rightarrow 2 \end{array}$	2060.068 4745.804	$4.6(-5) \\ -1.8(-4)$	$ 2.6(-5) \\ -6.8(-4) $	-2.3(-5) $-5.7(-5)$	-5.9(-8) $2.7(-4)$

Note. — Background-subtracted line luminosities for the subset of models with  $L_*=100$  L<sub> $\odot$ </sub>. In this table, a(b) means  $a\times 10^b$  L<sub> $\odot$ </sub>.

Table 7. Background-subtracted line luminosities

Species Transition	1 L <sub>⊙</sub>	10 L <sub>☉</sub>	$10^2~{ m L}_{\odot}$	$10^3~{ m L}_{\odot}$	$10^4~{ m L}_{\odot}$	$10^5~{ m L}_{\odot}$
<sup>12</sup> CO						
$J=1\rightarrow 0$	5.2(-3)	5.2(-3)	5.2(-3)	5.3(-3)	5.9(-3)	8.9(-3)
$4 \rightarrow 3$	1.2(-2)	1.3(-2)	1.5(-2)	2.8(-2)	7.5(-2)	1.7(-1)
$7 \rightarrow 6$	-1.0(-6)	3.9(-5)	1.2(-3)	1.4(-2)	8.9(-2)	3.3(-1)
$10 \rightarrow 9$	8.7(-7)	-1.1(-5)	-3.5(-5)	2.5(-3)	3.8(-2)	2.5(-1)
$13 \rightarrow 12$	4.8(-9)	2.5(-7)	-7.0(-5)	-5.1(-4)	6.1(-3)	9.9(-2)
$16 \rightarrow 15$	-8.6(-11)	3.0(-8)	-1.0(-5)	-4.4(-4)	-2.6(-3)	2.4(-2)
$19 \rightarrow 18$	-9.4(-11)	-3.6(-11)	-2.1(-7)	-1.2(-4)	-2.6(-3)	-7.8(-3)
$22 \rightarrow 21$	-6.1(-11)	-6.2(-11)	3.7(-9)	-1.5(-5)	-1.0(-5)	-1.2(-2)
$\mathrm{C}^{18}\mathrm{O}$						
$J=1\rightarrow 0$	1.0(-3)	1.0(-3)	1.1(-3)	1.1(-3)	1.3(-3)	1.5(-3)
$4 \rightarrow 3$	1.1(-4)	2.3(-4)	1.1(-3)	4.6(-3)	1.4(-2)	3.0(-2)
$7 \rightarrow 6$	9.7(-7)	8.2(-6)	1.2(-4)	1.3(-3)	8.4(-3)	3.2(-2)
$10 \rightarrow 9$	8.8(-9)	6.6(-7)	3.1(-6)	1.4(-4)	, ,	1.8(-2)
$13 \rightarrow 12$	-8.7(-11)	1.2(-8)	-2.9(-8)	-1.7(-5)	3.5(-4)	6.3(-3)
$16 \rightarrow 15$	-8.7(-11)	-2.6(-11)	7.1(-9)	-6.0(-6)	-1.9(-5)	1.5(-3)
$19 \rightarrow 18$	-9.4(-11)	-9.6(-11)	2.6(-10)	-7.1(-7)	-1.9(-5)	1.5(-4)
$22 \rightarrow 21$	-6.1(-11)	-6.2(-11)	-7.8(-11)	-4.8(-8)	-4.0(-6)	-3.1(-5)
$^{13}\mathrm{CO}$						
$J=1\rightarrow 0$	2.5(-3)	2.5(-3)	2.6(-3)	2.8(-3)	3.5(-3)	4.8(-3)
$4 \rightarrow 3$	5.0(-4)	7.4(-4)	2.4(-3)	1.0(-2)	3.3(-2)	7.8(-2)
$7 \rightarrow 6$	1.4(-6)	1.2(-5)	2.7(-5)	3.1(-3)	2.1(-2)	8.7(-2)
$10 \rightarrow 9$	4.3(-8)	1.4(-6)	-4.9(-6)	3.5(-4)	6.6(-3)	5.0(-2)
$13 \rightarrow 12$	-4.8(-11)	5.6(-8)	-2.4(-6)	-7.6(-5)	9.0(-4)	1.9(-2)
$16 \rightarrow 15$	-8.7(-11)	2.2(-10)	5.0(-9)	-2.8(-5)	-1.5(-4)	5.0(-3)
$19 \rightarrow 18$	-9.4(-11)	-9.6(-11)	1.7(-9)	-3.5(-6)	-9.3(-5)	5.6(-4)
$22 \rightarrow 21$	-6.1(-11)	-6.2(-11)	-4.3(-11)	-2.4(-7)	-2.0(-5)	-1.5(-4)
$0-H_2^{16}O$						
$1_{10} \xrightarrow{2} 1_{01}$	1.0(-3)	9.6(-4)	1.1(-3)	2.3(-3)	5.2(-3)	3.5(-3)
$3_{12} \rightarrow 3_{03}$			-5.0(-4)			
$3_{12} \rightarrow 2_{21}$			-2.4(-4)			

Table 7—Continued

Species						
Transition	$1~{\rm L}_{\odot}$	$10~{\rm L}_{\odot}$	$10^2~{\rm L}_{\odot}$	$10^3~{\rm L}_{\odot}$	$10^4~L_{\odot}$	$10^5~{\rm L}_{\odot}$
$3_{21} \rightarrow 3_{12}$	1.1(-6)	-1.6(-5)	-1.3(-4)	1.7(-3)	4.0(-2)	4.3(-1)
$2_{21} \rightarrow 2_{12}$	1.9(-4)	2.4(-5)	-2.1(-3)	-1.5(-2)	-5.1(-2)	-8.7(-2)
$2_{12} \to 1_{01}$	-2.0(-4)	-5.9(-4)	-5.3(-3)	-3.8(-2)	-1.9(-1)	-7.4(-1)
$3_{03} \rightarrow 2_{12}$	-6.2(-6)	-2.0(-4)	-2.8(-3)	-2.1(-2)	-9.6(-2)	-2.1(-1)
$2_{21} \rightarrow 1_{10}$	-3.1(-4)	-3.6(-4)	-2.5(-3)	-4.2(-2)	-4.0(-1)	-2.2(-0)
$3_{21} \rightarrow 2_{12}$	-1.8(-6)	-2.8(-6)	-2.6(-4)	-1.6(-2)	-3.4(-1)	-3.5(-0)
$o-H_2^{18}O$						
$1_{10}  1_{01}$	-7.8(-6)	-1.9(-5)	-2.5(-5)	-8.3(-5)	-9.0(-5)	7.0(-4)
$3_{12} \rightarrow 3_{03}$	2.5(-8)	5.4(-8)	-4.3(-6)	1.8(-4)	2.7(-3)	1.8(-2)
$3_{12} \rightarrow 2_{21}$	1.2(-9)	-4.6(-9)	-8.7(-7)	6.2(-5)	6.7(-4)	4.6(-3)
$3_{21} \rightarrow 3_{12}$	5.7(-9)	4.8(-7)	1.2(-5)	3.4(-4)	4.0(-3)	2.5(-2)
$2_{21} \rightarrow 2_{12}$	4.3(-8)	-8.1(-6)	-1.3(-4)	-1.0(-3)	-4.7(-3)	-1.8(-2)
$2_{12} \rightarrow 1_{01}$	-2.8(-5)	-2.6(-4)	-2.6(-3)	-1.5(-2)	-5.5(-2)	-1.4(-1)
$3_{03} \rightarrow 2_{12}$	-2.4(-7)	-1.7(-5)	-3.2(-4)	-2.4(-3)	-7.6(-3)	-1.0(-2)
$2_{21} \rightarrow 1_{10}$	-3.9(-7)	-1.8(-5)	-7.3(-4)	-9.6(-3)	-5.5(-2)	-1.8(-1)
$3_{21} \rightarrow 2_{12}$	-1.3(-9)	-4.7(-8)	-2.1(-5)	-1.5(-3)	-2.8(-2)	-2.0(-1)
$p-H_2^{16}O$						
$3_{13} \rightarrow 2_{20}$	3.0(-8)	7.4(-7)	5.5(-6)	4.0(-5)	2.5(-4)	7.0(-4)
$2_{11} \rightarrow 2_{02}$	3.9(-6)	-7.4(-6)	1.1(-4)	2.5(-3)	2.5(-2)	1.8(-2)
$2_{02} \rightarrow 1_{11}$	-1.6(-5)	-1.8(-4)	-8.2(-4)	-8.4(-4)	2.4(-2)	4.6(-3)
$1_{11} \rightarrow 0_{00}$	-6.0(-4)	-1.1(-3)	-3.8(-3)	-1.5(-2)	-5.3(-2)	2.5(-2)
$2_{20} \rightarrow 2_{11}$	7.3(-6)	-5.8(-5)	-5.5(-4)	-1.0(-4)	3.6(-2)	-1.8(-2)
$3_{22} \rightarrow 3_{13}$	-3.2(-8)	-1.4(-5)	-5.1(-4)	-6.0(-3)	-2.9(-2)	-1.4(-1)
$3_{13} \rightarrow 2_{02}$				-2.6(-2)		
	-2.2(-5)					
$3_{22} \rightarrow 2_{11}$	-2.9(-9)	-3.1(-6)	-4.8(-4)	-1.8(-2)	-2.6(-1)	-2.0(-1)
$p-H_2^{18}O$						
$3_{13} \rightarrow 2_{20}$	-5.6(-10)	1.8(-9)	2.2(-8)	5.1(-7)	1.0(-5)	7.0(-4)
$2_{11} \rightarrow 2_{02}$	6.7(-7)	5.7(-6)	6.2(-5)	6.0(-4)	3.1(-3)	1.8(-2)
$2_{02} \rightarrow 1_{11}$	-5.9(-7)	-9.5(-6)	-4.4(-6)	5.8(-4)	4.7(-3)	4.6(-3)
$1_{11} \rightarrow 0_{00}$	-4.6(-5)	-2.6(-4)	-1.3(-3)	-4.1(-3)	-9.3(-3)	2.5(-2)

Table 7—Continued

Species Transition	$1~{\rm L}_{\odot}$	$10~{\rm L}_{\odot}$	$10^2~{\rm L}_{\odot}$	$10^3~{ m L}_{\odot}$	$10^4~{ m L}_{\odot}$	$10^5~{ m L}_{\odot}$
$2_{20} \rightarrow 2_{11}$ $3_{22} \rightarrow 3_{13}$ $3_{13} \rightarrow 2_{02}$ $2_{20} \rightarrow 1_{11}$ $3_{22} \rightarrow 2_{11}$	2.4(-8) $-1.9(-10)$ $-2.5(-8)$ $-2.5(-8)$ $-9.0(-11)$	5.8(-7) $-7.1(-8)$ $-4.3(-6)$ $-4.1(-6)$ $-3.5(-8)$	3.6(-5) $-4.9(-6)$ $-1.5(-4)$ $-2.8(-4)$ $-9.8(-6)$	6.9(-4) $-3.5(-5)$ $-1.6(-3)$ $-5.2(-3)$ $-4.9(-4)$	4.8(-3) $-3.5(-6)$ $-7.9(-3)$ $-3.8(-2)$ $-6.8(-3)$	-1.8(-2) $-1.4(-1)$ $-1.0(-2)$ $-1.8(-1)$ $-2.0(-1)$
$ \begin{array}{c} 16O\\ 0 \to 1\\ 1 \to 2 \end{array} $	-3.1(-9) $-2.4(-6)$	-1.2(-7) $-2.5(-6)$	-2.3(-5) $-5.7(-5)$	-4.3(-4) $-6.0(-3)$	$ \begin{array}{c} 1.7(-3) \\ -1.8(-1) \end{array} $	$ 8.6(-2) \\ -2.0(-0) $

Note. — line luminosities for the subset of models with  $M_{0.1}=100~{\rm M}_{\odot}$ . In this table, a(b) means  $a\times 10^b~{\rm L}_{\odot}$ . See Table 6 for rest frequencies.

Table 8: Maximum upper rotational quantum number,  $J_u$ , for any  $^{12}\mathrm{CO}$  emission line.

$M_{0.1}/{ m M}_{\odot}$	$1~{\rm L}_{\odot}$	$10~\mathrm{L}_\odot$	$10^2~{\rm L}_{\odot}$	$10^3~{\rm L}_{\odot}$	$10^4~{\rm L}_{\odot}$	$10^5~{\rm L}_{\odot}$	$10^6~{\rm L}_{\odot}$
1	24	24	24				_
10	22	24	24	24			_
$10^{2}$	$13^{a}$	$18^{b}$	$24^c$	11	14	17	_
$10^{3}$	8	5	5	7	9	11	12

<sup>&</sup>lt;sup>a</sup> Transitions with  $J_u = 7$  and 8 are absorption lines

<sup>&</sup>lt;sup>b</sup> Transitions with  $8 \le J_u \le 12$  are absorption lines

<sup>&</sup>lt;sup>c</sup> Transitions with  $9 \le J_u \le 20$  are absorption lines

Table 9: Target water lines for high-z extra-galactic sources

	Rest	Redshifted	Frequency	
	Frequency	F10214+4724	Cloverleaf	BR1202-0725
Transition	(GHz)	z=2.286	z=2.551	z=4.702
$2_{11} \rightarrow 2_{02}$	752.0	228.9	211.8	131.9
$2_{02} \rightarrow 1_{11}$	987.9			173.2
$3_{12} \rightarrow 3_{03}$	1097			192.4
$1_{11} \rightarrow 0_{00}$	1113			195.3
$3_{12} \rightarrow 2_{21}$	1153			202.2
$3_{21} \rightarrow 3_{12}$	1163			203.9
$2_{20} \rightarrow 2_{11}$	1229			215.5

Table 10: Effective  $^{12}$ CO and  $\mathrm{H}_2^{16}$ O column densities, for the v=2-0 and  $\nu_2$  absorption bands respectively. In this table a(b) means  $a\times 10^b\,\mathrm{cm}^{-2}$ .

Species	$M_{0.1}/M_{\odot}$	$1~{ m L}_{\odot}$	$10~{\rm L}_{\odot}$	$10^2~{\rm L}_{\odot}$	$10^3~{\rm L}_{\odot}$	$10^4~{\rm L}_{\odot}$	$10^5~{ m L}_{\odot}$	$10^6~{ m L}_{\odot}$
СО	1	1.0(19)	3.4(19)	4.9(19)		_	_	_
	10	1.4(18)	1.3(18)	2.2(18)	1.2(20)			
	60						1.1(20)	
	$10^{2}$	2.9(18)	2.9(18)	2.9(18)	2.8(18)	1.1(19)	1.5(20)	
	$10^{3}$	5.7(18)	5.7(18)	5.7(18)	5.7(18)	5.6(18)	5.4(18)	5.3(19)
$H_2O$	1	5.0(16)	1.5(17)	5.9(18)				
	10	3.8(16)	3.7(16)	3.0(17)	9.2(18)			
	60						1.4(19)	
	$10^{2}$	9.4(16)	9.4(16)	9.4(16)	9.1(16)	1.5(18)	8.1(18)	
	$10^{3}$	2.1(17)	2.1(17)	2.1(17)	2.1(17)	2.1(17)	2.0(17)	1.6(18)

#### REFERENCES

Abgrall, H. Le Bourlot, J., Pineau des Forets, G., Roueff, E., Flower, D. R., & Heck, L. 1992, A&A, 253, 525

Barvainis, R., Antonucci, R., & Coleman, P. 1992, ApJ, 399, L19

Barvainis, R., Tacconi, L., Antonucci, R., Alloin, D., & Coleman, P. 1994, Nature, 371, 586

Bohlin, R. C., Savage, B. D., & Drake, J. F. 1978, ApJ, 224, 132

Brown, R. L., & Vanden Bout, P. A. 1991, AJ, 102, 1956

Carr, J. S., Evans, N. J. II, Lacy, J. H., & Zhou, S. 1995, ApJ, 450, 667

Ceccarelli, C., Hollenbach, D. J., & Tielens, A. G. G. M. 1996, ApJ, 471, 400 (CHT)

Cernicharo, J., Gonzalez-Alfonso, E., Alcolea, J., Bachiller, R., & John D. 1994, ApJ, 432, L59

Cernicharo, J., Thum, C., Hein, H., John, D., Garcia, P., & Mattioco, F. 1990, A&A, 231, L15

Doty, S. D. 1997, in preparation

Doty, S. D., & Neufeld, D. A. 1997, in preparation

Downes, D., Solomon, P. M., & Radford, S. E. J. 1993, ApJ, 414, L13

Draine, B. T., & Lee, H. M. 1987, ApJ, 318, 485

Egan, M. P., Leung, C. M., & Spagna, G. F., Jr. 1988, Comput. Phys. Comm., 48, 271

Erickson, E. F. et al. 1977, ApJ, 212, 696

Fuller, G. A., & Myers, P. C. 1993, ApJ, 418, 273

Gensheimer, P., Mauersberger, R., & Wilson, T. L. 1996, A&A, in press

Genzel, R., & Stutzki, J. 1989, ARAA, 27, 41

Goldsmith, P. F., & Langer, W. D. 1978, ApJ, 222, 881

Goldsmith, P. F., Langer, W. D., Schloerb, F. P., & Scoville, N. Z. 1980, ApJ, 240, 524

Green, S., Maluendes, S., & McLean, A. D. 1993, ApJS, 85, 181

Helmich, F. P., van Dishoeck, E. F., Black, J. H., & de Graauw, Th. 1996, A&A, in press

Hewitt, A., Burbidge, G. 1989 in "A New Optical Catalog of Quasi-Stellar Objects"

Hollenbach, D. J., & McKee, C. F. 1989, ApJ, 342, 306

Jacq, T., Jewell, P. R., Henkel, C., Walmsley, C. M., & Baudry, A. 1988, A&A, 199, L5

Keto, E. R., Ho, P. T. P., & Haschick, A. D. 1988, ApJ, 324, 920

Larson, R. B. 1969, MNRAS, 145, 271

Mathis, J. S., Mezger, P. G., & Pangia, N.1983, A&A, 128, 212

Millar, T. J., Rawlings, J. M. C., Bennett, A., Brown, P. D., & Charnley, S. B. 1991, A&AS, 87, 585

Mitchell, G. F., Curry, C., Maillard, J.-P., Allen, M., 1989, ApJ, 341, 1020

Mitchell, G. F., Maillard, J.-P., Allen, M., Beer, R., Belcourt, K., 1990 ApJ, 363, 554

Mozurkewich, D., Schwartz, P. R., & Smith, H. A. 1986, ApJ, 311, 371

Myers, P. C., & Fuller, G. A. 1992, ApJ, 396, 631

Neufeld, D. A., & Green, S. 1994, ApJ, 432, 158

Neufeld, D. A., & Kaufman, M. J. 1993, ApJ, 418, 263 (NK)

Neufeld, D. A., Lepp, S., & Melnick, G. J. 1995, ApJS, 100, 132 (NLM)

Petitjean, P., Pecontal, E., Valls-Gabaud, D., & Charlot, S. 1996, Nature, 380, 411

Phillips, T. R. & Green, S. 1995, Ap&SS, 224, 537

Phillips, T. G., Kwan, J., & Huggins P. J. 1980, in "Interstellar Molecules", ed. B.H. Andrew, Reidel, Dordrecht, Holland, p21.

Rybicki, G. B., & Hummer, D. G. 1992, A&A, 262, 209

Shu, F. H. 1977, ApJ, 214, 488

Shu, F. H., Adams, F. C., & Lizano, S. 1987, ARAA, 25, 23

Takahasi, T., Hollenbach, D. J., & Silk, J. 1983, ApJ, 275, 145

Tauber, J., Olofsson, G., Pilbratt, G., Nordh, L., & Frisk, U. 1996, A&A, 308, 913

van Dishoeck, E. F., & Helmich, F. P. 1996, A&A, in press (vDH)

Wannier, P. G., Pagani, L., Kuiper, T. B. H., Frerking, M. A., Gulkis, S., Encrenaz, P., Pickett, H. M., Lecacheux, A., & Wilson, W. J. 1991, ApJ, 377, 171

Waters, J. W., Gustincic, J. J., Kakar, R. K., et al. 1980, ApJ, 235, 57

Whittet, D. C. B. 1992, "Dust in the Galactic Environment", IOP Publishing, Ltd.

Zmuidzinas, J., Blake, G. A., Carlstrom, J., Keene, J., Miller, D., & Schilke, P. 1996, ApJ, submitted

This preprint was prepared with the AAS IATEX macros v4.0.

- Fig. 1.— Schematic representation of the model presented in this paper.
- Fig. 2.— Comparison of the predicted dust continuum spectrum for the standard model (solid line) with observations of the Orion Molecular Cloud 1 (symbols).
- Fig. 3.— Dust (dashed line) and gas (solid line) temperature distributions for the standard model.
- Fig. 4.— Fractional abundances of  $^{12}C^{16}O$ , atomic oxygen, and o- $H_2^{16}O$  relative to  $H_2$ , as functions of position in our standard model.
- Fig. 5.— Cooling coefficient  $(\Lambda/n[H_2]^2)$  for a variety of species in our standard model.
- Fig. 6.— Line luminosities for the three isotopes of CO, as a function of upper rotational quantum number for our standard model.
- Fig. 7.— Continuum and line ( $^{12}$ CO,  $H_2^{16}$ O, and OI) spectrum for the standard model, assuming D = 1 kpc and a resolution of  $\lambda/\Delta\lambda = 10^4$ .
- Fig. 8.— Line profiles for the nine transitions of ortho- $H_2^{16}O$  included in our standard model. The vertical axis shows the monochromatic luminosity.
- Fig. 9.— Same as Figure 8, but for transitions of ortho- $H_2^{18}$ O.
- Fig. 10.— Same as Figure 8, but for transitions of para-H<sub>2</sub><sup>16</sup>O and atomic oxygen.
- Fig. 11.— Same as Figure 8, but for transitions of para- $H_2^{18}$ O.
- Fig. 12.— Gas (solid lines) and dust (dashed lines) temperature distributions for all models in our grid. Each box corresponds to a given value of  $M_{0.1}$ , and each curve is labeled by  $\log_{10}(L_*)$ .
- Fig. 13.— Line strengths for selected  $^{12}$ CO transitions for the grid of models considered in the text. The upper panel of each box corresponds to emission for a given transition, while the lower panel of the same box corresponds to absorption for the same transition. The different symbols correspond to different core masses  $(M_{0.1})$ : the open triangles, open squares, crosses, and open circles correspond to  $M_{0.1} = 1$ , 10,  $10^2$ , and  $10^3$  M<sub> $\odot$ </sub> respectively. Each box is labeled with the molecular transition to which it refers.
- Fig. 14.— Same as Figure 13, but for transitions of ortho-H<sub>2</sub><sup>16</sup>O.
- Fig. 15.— Same as Figure 13, but for transitions of ortho- $\mathrm{H}_{2}^{18}\mathrm{O}.$

- Fig. 16.— Same as Figure 13, but for transitions of para- $\mathrm{H}_{2}^{16}\mathrm{O}.$
- Fig. 17.— Same as Figure 13, but for transitions of para- $\mathrm{H}_2^{18}\mathrm{O}$  and atomic oxygen.
- Fig. 18.—  $^{12}{\rm CO}$  emission line luminosity as a function of upper rotational quantum number,  $J_u,$  for various value of the core mass,  $M_{0.1}.$  Results apply to cloud cores in which the central luminosity  $L_*=100\,{\rm L}_{\odot}.$

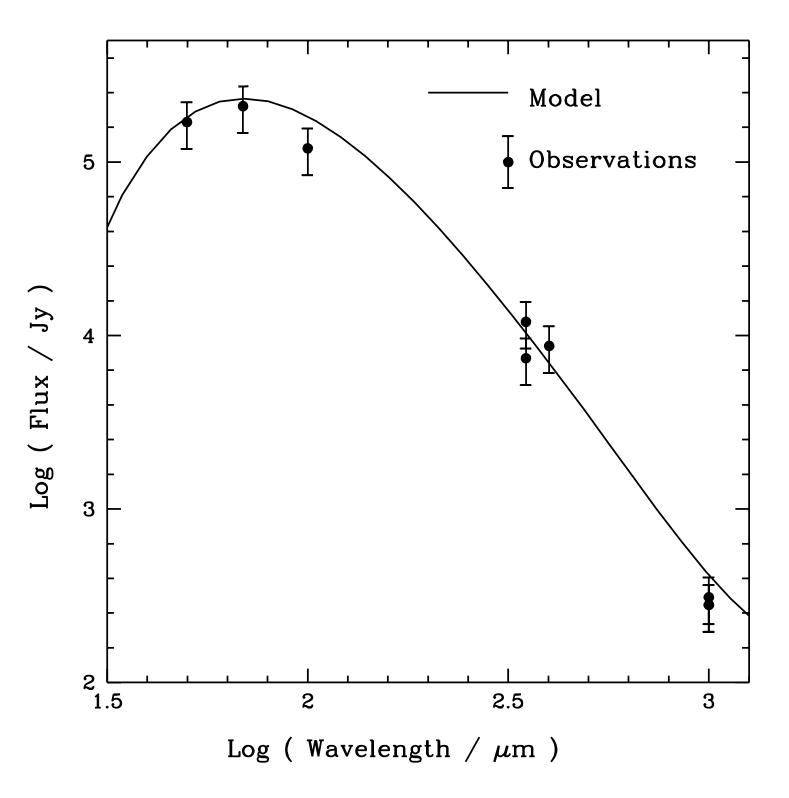
Choose core mass (M) and Central Luminosity (L)

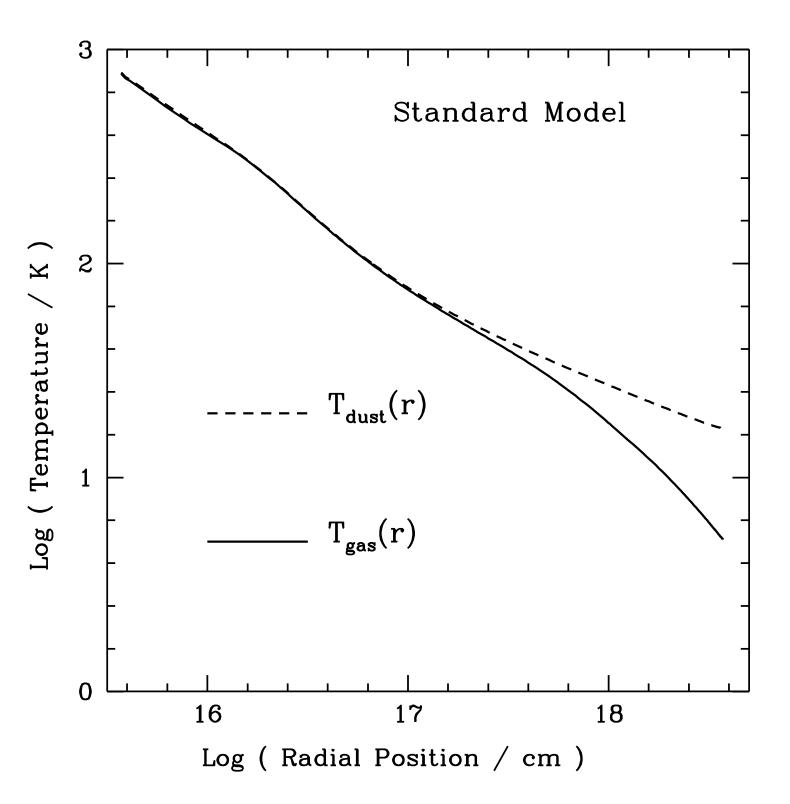
Determine density profile (n[r]) and line width ∆v (Hydrostatic equilibrium)

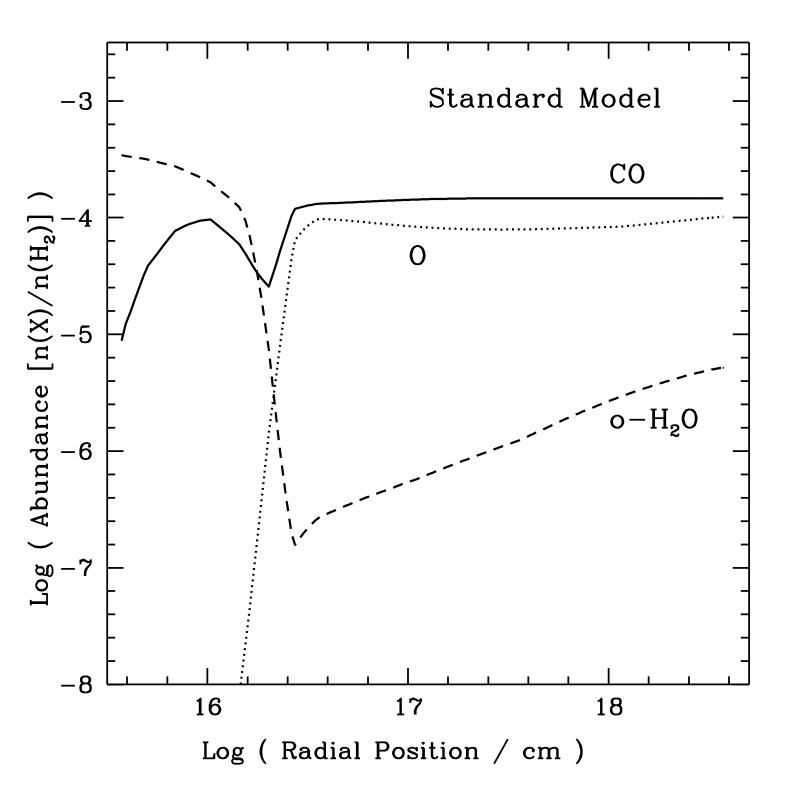
Determine dust temperature profile (Tdust[r]) (Continuum radiative transfer)

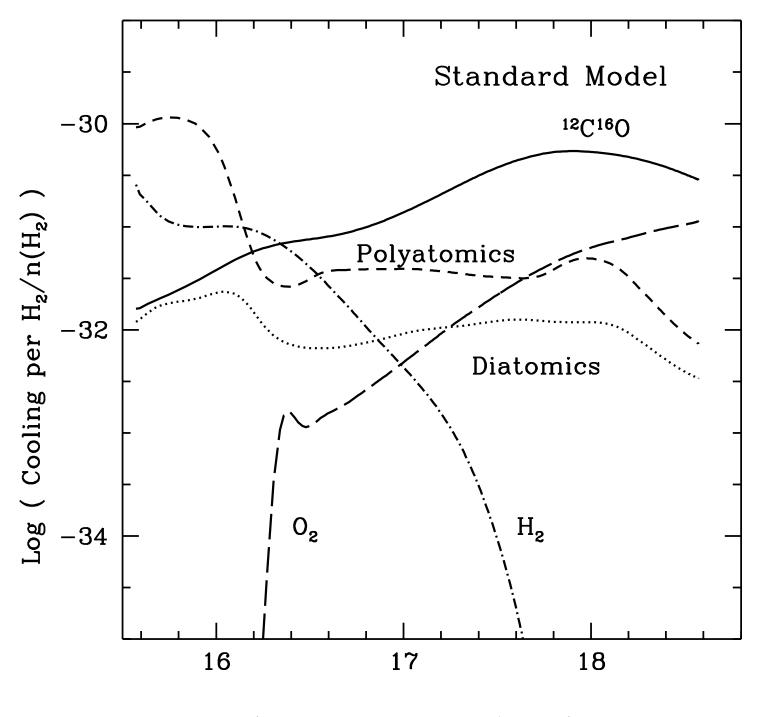
Determine gas temperature profile (Tgas[r]) and molecular abundances (Thermal balance; Chemistry)

Compute line strengths and profiles (Line transfer [ALI method])

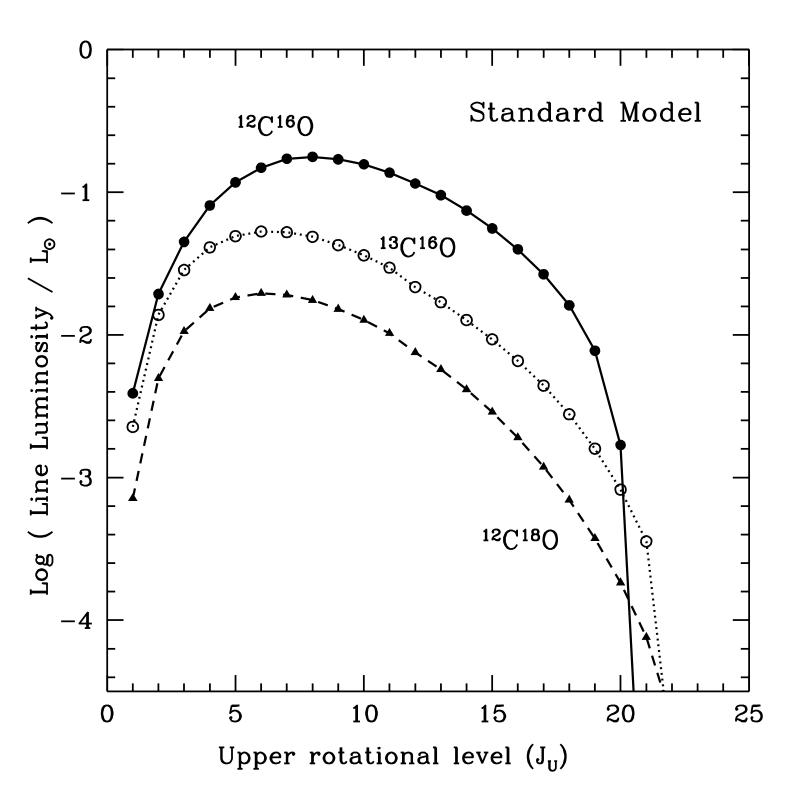


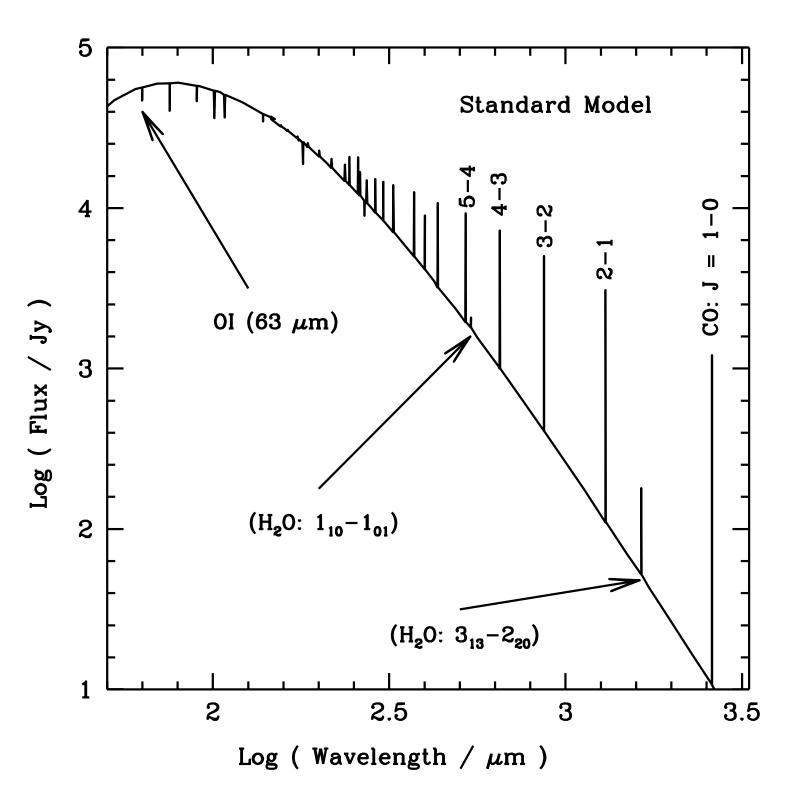


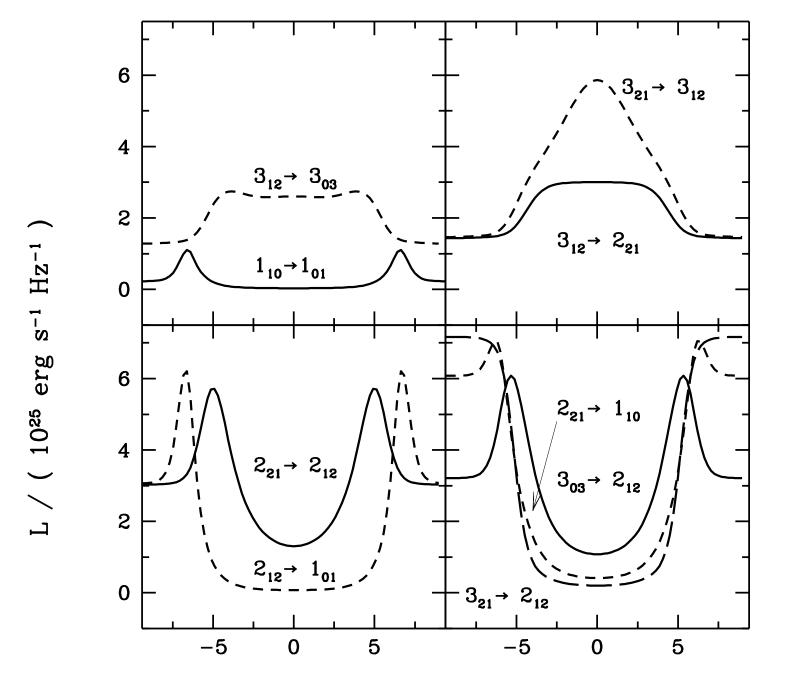




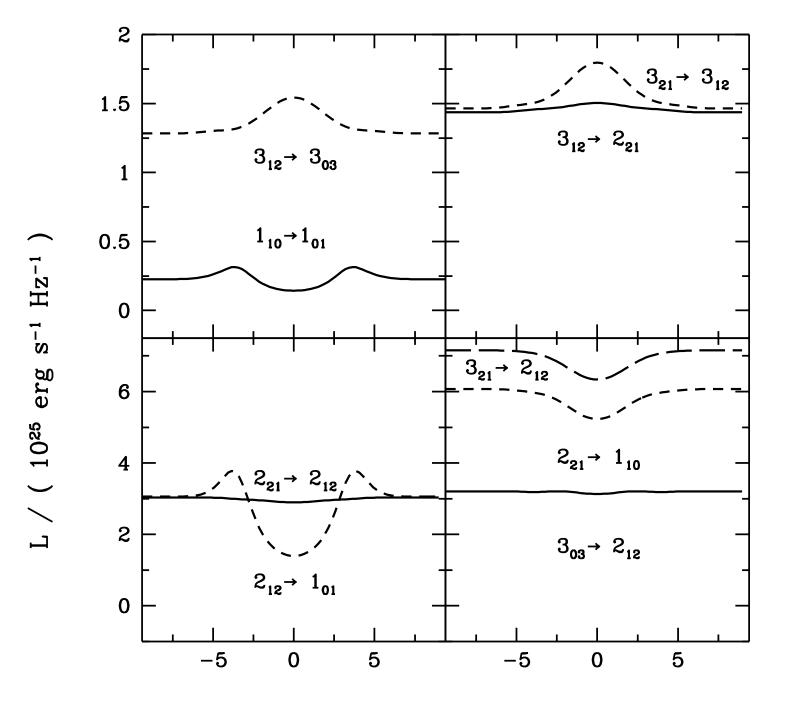
Log (Radial Position / cm)



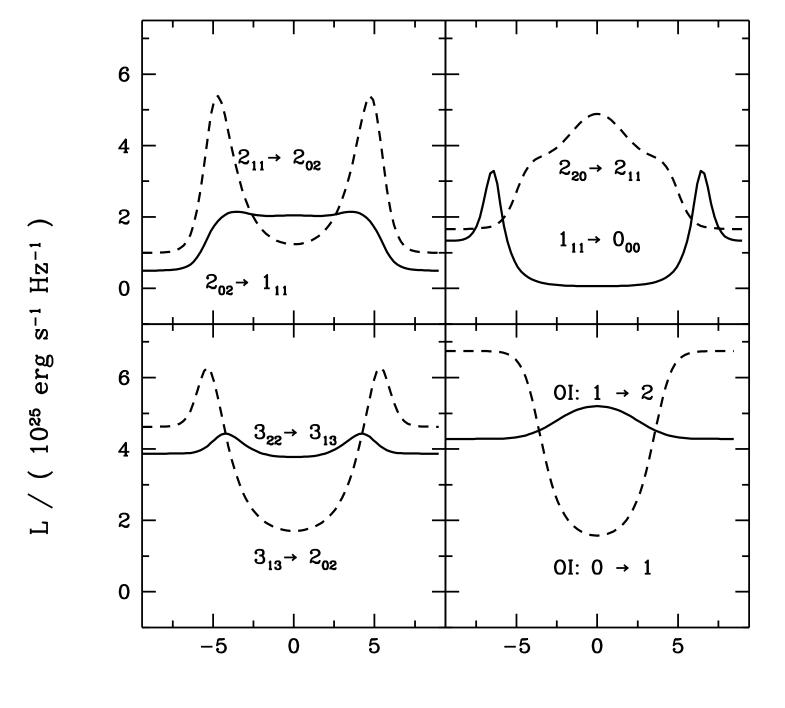




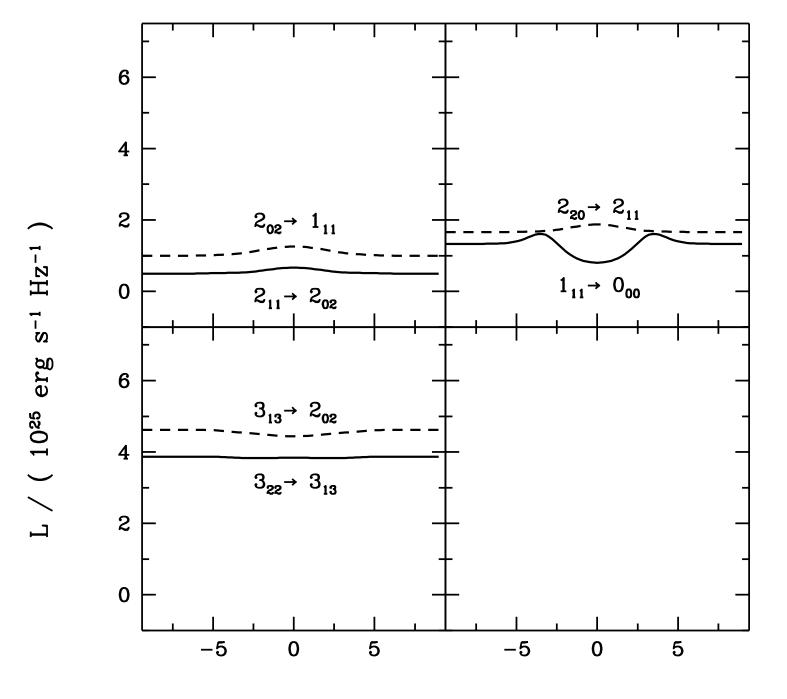
Doppler Velocity / ( km s<sup>-1</sup> )



Doppler Velocity / ( km s<sup>-1</sup> )



Doppler Velocity / ( km s<sup>-1</sup> )



Doppler Velocity / ( km s<sup>-1</sup> )

